Journal of the Optical Society of America A
OPTICS, IMAGE SCIENCE, AND VISION

Phaseless inverse scattering for rough surface recovery at a single receiver

YUXUAN CHEN,[1,*] MARK SPIVACK,[2] AND ORSOLA RATH SPIVACK[2]

[1]School of Mathematical Sciences, Soochow University, Suzhou, China
[2]Department of Applied Mathematics and Theoretical Physics, University of Cambridge, Cambridge, UK
*yc397@cantab.ac.uk

Received 19 January 2026; revised 31 March 2026; accepted 31 March 2026; posted 31 March 2026; published 24 April 2026

We present a reconstruction algorithm for recovering rough surface profiles from phaseless total field data measured at a single receiver as the surface undergoes controlled lateral motion. The algorithm is based on the parabolic wave equation, which offers a computationally efficient framework for forward and inverse scattering, and applies to both Dirichlet (TE polarization) and Neumann (TM polarization) boundary conditions. It operates in a marching fashion, recovering surface points sequentially along the profile. Numerical experiments demonstrate that the method yields accurate reconstructions and remains robust under measurement noise and variations in key problem parameters. The proposed approach provides a reliable and efficient tool for surface characterization in engineering applications such as non-destructive testing and remote sensing.

https://doi.org/10.1364/JOSAA.590051

1. INTRODUCTION

The reconstruction of rough surfaces from scattered data has gained considerable attention due to its critical applications in various fields such as remote sensing, geophysical radar systems, non-destructive testing, and the study of dynamic ice sheets and glaciers [1–6]. These applications require accurate surface reconstruction for precise environmental monitoring, effective structural health assessment, and reliable climate research. There have been a number of methods for inverse surface scattering; common approaches include the Kirchhoff approximation [7], the Rytov approximation [8], iterative schemes [9,10], Newton-type methods [11–14], sampling-based techniques [15,16], methods based on Kirchhoff integral equations [17,18], and, in particular, algorithms based on the parabolic wave equation [19,20]. These conventional methods often rely on extensive scattered field measurements that include phase information. However, two major limitations hinder their practical applicability. First, the requirement for extensive scattered data necessitates the use of numerous signal receivers, which may cause complex interference issues with measurement data. Second, the need for phase information poses a significant difficulty, as obtaining accurate phase data is usually impractical in most real-world applications.

These challenges have motivated the development of alternative strategies that reduce the data requirements while maintaining reconstruction accuracy. Several studies have explored the recovery of rough surface profiles using phaseless data, namely relying only on the amplitude of the field data (see e.g., [21–26]). In these approaches, the reconstruction is typically based on intensity-only measurements collected over an observation line or plane, often requiring multiple observation points or measurement positions, so that a relatively large number of receivers is still needed. In particular, our previous work [27] proposed a novel algorithm for reconstructing rough surfaces using a single receiver by moving the measurement apparatus relative to the surface, but it still required access to the full scattered field, including phase information. This approach demonstrated accurate and robust performance, highlighting the potential for simplifying the data requirements. Motivated by this, the present work seeks to eliminate the need for phase information altogether while retaining the single-receiver setting, thereby working with significantly more limited data than existing phaseless approaches.

In this paper, we develop an algorithm to recover rough surface profiles from phaseless total field data measured at a single receiver. The surface is illuminated by a time-harmonic Gaussian beam, and the amplitude of the total field is recorded at a fixed location while the surface undergoes controlled lateral motion. This moving-surface configuration allows more geometric information to be extracted from limited data and is inspired by practical non-destructive testing setups. The reconstruction is formulated under the parabolic wave equation, which provides a computationally efficient framework for both forward and inverse scattering problems. The method is applied to both Dirichlet and Neumann boundary conditions on the rough surface, which correspond to TE and TM polarizations in electromagnetic scattering. For clarity, the main differences between the present method and our previous related methods,

Table 1. Comparison of Problem Setups across Different Methods

Problem Setups	Ref. [21]	Ref. [27]	Present Work
Phaseless data (no phase measurement needed)	✓	✗	✓
Single receiver (minimal sensor setup)	✗	✓	✓
Moving surface (non-destructive testing setup)	✗	✓	✓
Marching algorithm (sequential reconstruction)	✓	✓	✓

all formulated under the parabolic wave equation framework, in terms of problem setup, are summarized in Table 1. As seen from the table, the present method is the only one that simultaneously achieves phaseless data acquisition and a single-receiver moving-surface configuration, representing a significant advancement beyond the previous approaches where these features were treated separately.

The proposed reconstruction method follows a pointwise marching strategy along the surface. At each reconstruction stage, the rough surface is shifted to the left, and a new surface point is recovered at the rightmost end of the domain. The algorithm consists of two main steps at each stage: first, the surface current is computed by solving a lower-triangular linear system derived from the parabolic integral equations; second, the surface height at the receiver point is reconstructed from the obtained current and measured phaseless data. This process is repeated sequentially, enabling the entire rough segment to be reconstructed from left to right. In effect, this approach combines the key elements of the previous related methods [21,27]. The present approach updates the surface current matrix sequentially using the successively recovered surface information during the marching process, rather than using an iterative or simplified treatment.

A series of numerical experiments are conducted to validate the effectiveness of the proposed method. The reconstruction results show a close match between the recovered and true surface profiles in both TE and TM polarizations. Through further numerical examples, the algorithm also demonstrates robustness under various levels of white noise and maintains reliable performance across different problem parameters, including receiver height, discretization size, and surface scale. In addition, a direct comparison with our previous full-field method [27] under the same setting is included to demonstrate that the present method achieves comparable reconstruction accuracy despite relying only on phaseless data.

The remainder of the paper is structured as follows. In Section 2, we introduce the mathematical formulation of the forward scattering problem based on the parabolic wave equation for TE and TM polarizations. Section 3 presents the proposed reconstruction algorithm, including the marching strategy and two-step recovery process. In Section 4, a range of numerical experiments are presented to demonstrate the accuracy and robustness of the proposed method under various conditions. Finally, Section 5 concludes the paper with a summary and discussion of potential extensions.

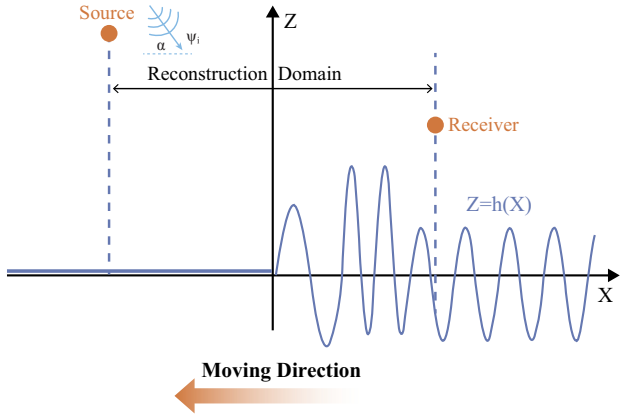

Fig. 1. Wave scattering from a rough surface illuminated by an incident wave.

2. MATHEMATICAL FORMULATIONS AND PROBLEM SETTING

We investigate the electromagnetic wave scattering from a one-dimensional rough surface, as depicted in Fig. 1.

The problem is formulated in a two-dimensional coordinate system, where the horizontal and vertical axes are denoted by x and z, respectively. The rough surface, represented by $z = h(x)$, is modeled as a perfectly electric conducting (PEC) boundary. In this study, the rough surface is considered to be a rough segment confined to the interval $x \in [0, L]$, representing a localized portion of a conceptually extended surface. A point source is positioned at $x = 0$ to serve as the incident field. Our objective is to reconstruct the surface profile from the phaseless total field data (i.e., the magnitude of the field) measured at a single field receiver.

Surface scattering problems are traditionally formulated using the time-harmonic scalar wave equation, with most studies based on the full Helmholtz equation [2,28,29]. In this work, we assume a small incident angle (i.e., the grazing angle case) and dominant forward wave propagation, in which case the Helmholtz equation can be approximated by the parabolic wave equation [30–32]. In this section, we first review the parabolic integral formulations and then establish the specific setup for the proposed surface reconstruction algorithm.

A. Integral Formulations

Let $p(\mathbf{r})$ denote the time-harmonic scalar wave field at the point $\mathbf{r} = (x, z)$. Under the regime described by the parabolic wave equation, we introduce the field $\psi(\mathbf{r})$, given by $\psi(\mathbf{r}) = p(\mathbf{r}) \exp(-ikx)$, where k is the wavenumber associated with the incident wave, with λ being the wavelength. The field $\psi(\mathbf{r})$ predominantly propagates along the x axis via factoring out the primary oscillatory behavior in the x direction. Substituting this into the Helmholtz equation and neglecting the second-order derivative in x, we obtain the parabolic wave equation [30–32]:

$$\frac{\partial \psi}{\partial x} = \frac{i}{2k} \frac{\partial^2 \psi}{\partial z^2}. \tag{1}$$

Let Γ represent the space of the rough surface, defined by $\Gamma := \{(x, z) : z = h(x), 0 \le x \le L\}$, and V^+ be the upper

medium, $V^+ = \{(x, z)|z > h(x), 0 \le x \le L\}$. If applying the Green's theorem to the parabolic wave equation, the scattered field in V^+ can be expressed in the form of a pair of coupled integral equations, which relate the surface current (denoted by J or K based on polarization). Two cases based on the boundary conditions are considered: the Dirichlet boundary condition corresponding to the transverse electric (TE) polarization and the Neumann boundary condition corresponding to the transverse magnetic (TM) polarization. To distinguish between cases, the field ψ is replaced by E and H to denote the electric and magnetic fields, respectively.

For the TE field, the wave satisfies the Dirichlet boundary condition, where the electric field vanishes on the surface, i.e., $E|_\Gamma = 0$, and the surface current is given by $J = \partial E/\partial z|_\Gamma$. The coupled integral equations for the electric field E are

$$E_i(\mathbf{r}) = -\int_0^x G(\mathbf{r}; \mathbf{r}')J(\mathbf{r}')\,\mathrm{d}x', \quad \mathbf{r}, \mathbf{r}' \in \Gamma, \tag{2a}$$

$$E_s(\mathbf{q}) = \int_0^x G(\mathbf{q}; \mathbf{r})J(\mathbf{r}')\,\mathrm{d}x', \quad \mathbf{q} \in V^+, \mathbf{r}' \in \Gamma, \tag{2b}$$

where E_i and E_s denote the incident and scattered electric fields, respectively, J represents the surface current, and G is the Green's function of the parabolic equation in the free space, given by

$$G(x, z; x', z') = \frac{1}{2}\sqrt{\frac{i}{2\pi k}}\frac{1}{\sqrt{x - x'}}\exp\left[\frac{ik(z - z')^2}{2(x - x')}\right]. \tag{3}$$

For the TM case, the wave satisfies the Neumann boundary condition, where the normal derivative of the magnetic field vanishes on the surface, i.e., $\partial H/\partial z|_\Gamma = 0$, and the surface current corresponds to the surface wave field, given by $K = H|_\Gamma$. The coupled integral equations for the magnitude field H are

$$H_i(\mathbf{r}) = \int_0^x \frac{\partial G(\mathbf{r}; \mathbf{r}')}{\partial z'}K(\mathbf{r}')\,\mathrm{d}x', \quad \mathbf{r}, \mathbf{r}' \in \Gamma, \tag{4a}$$

$$H_s(\mathbf{q}) = -\int_0^x \frac{\partial G(\mathbf{q}; \mathbf{r}')}{\partial z'}K(\mathbf{r}')\,\mathrm{d}x', \quad \mathbf{q} \in V^+, \mathbf{r}' \in \Gamma, \tag{4b}$$

where H_i and H_s are incident and scattered magnetic fields, respectively, K represents the surface current, and G is the Green's function defined in Eq. (3).

B. Problem Setting

In this study, the objective is to reconstruct the profile of a rough surface from the phaseless total field data measured at a single receiver. To do this, the reconstruction is carried out as the surface moves toward the negative x direction. It is important to note that this configuration is equivalent to a setup where the source and receiver move relative to a stationary surface, as commonly encountered in non-destructive testing experiments. This setup is the same as the one used in our earlier work based on non-phaseless data [27]. We consider an extended surface composed of two parts: a flat region ($h = 0$) and a rough region, where the rough segment is the primary focus of interest. The length between the source and the receiver is fixed at L, while the total length of the extended surface is set to be $2L$ with the flat and rough segments each occupying a length of L within this domain.

In the initial configuration, the flat segment lies in $[0, L]$, and the rough part occupies $(L, 2L]$. The point source and the receiver are positioned at $(0, \zeta)$ and (L, z_0), respectively. The entire domain $[0, 2L]$ is discretized into $2N+1$ points with $x_n = n\Delta x$, where $n = 0, 1, 2, \ldots, 2N$. The distance Δx is chosen to satisfy the condition: $\Delta x \le \lambda/10$, where λ is the wavelength, ensuring that each wavelength is adequately resolved by at least 10 discrete points.

The reconstruction algorithm proceeds as the surface shifts leftward (along the negative x axis). To describe this process, we introduce discrete *reconstruction stages* indexed by t_j, where $j = 0, 1, \ldots, N$. Suppose that the initial configuration corresponds to the stage t_0, and at each subsequent stage, the surface shifts by Δx distance to the left, i.e., from t_j to t_{j+1}. At each reconstruction stage, the coordinate system is re-centered such that the source and receiver remain fixed at $(0, \zeta)$ and (L, z_0), respectively. As the surface moves, we denote the surface profile at stage t_j by $h_j(x)$ with

$$h_j(x) = h_0(x + j\Delta x), \quad x \in [0, L]. \tag{5}$$

An illustration of the reconstruction configuration is shown in Fig. 2.

Clearly, at the final stage t_N, the entire rough segment of interest lies in the domain $[0, L]$. We denote the entire rough surface over this interval as $h_r(x)$, given by

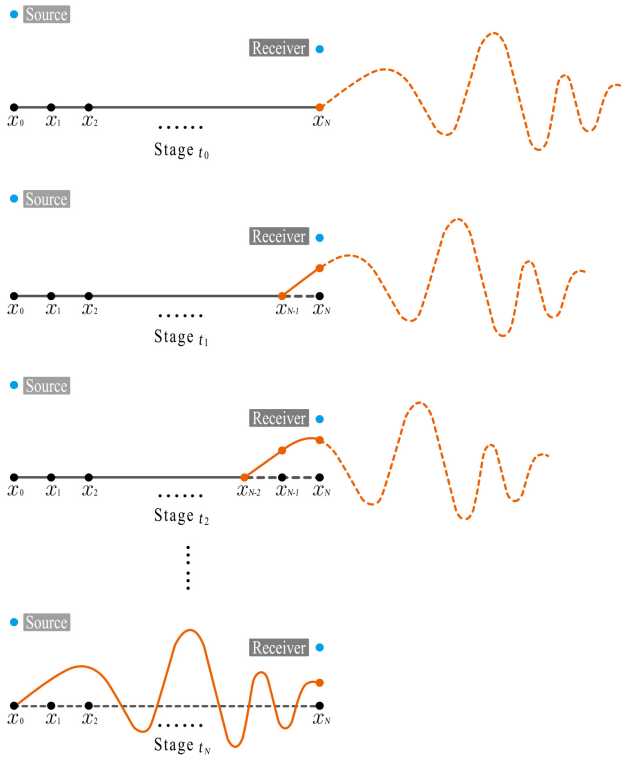

Fig. 2. Illustration of reconstruction stages. There are totally N stages indexed by t_j, where $j = 1, 2, \ldots, N$. In each stage, the reconstruction is performed over the fixed domain between the source and the receiver, i.e., $x_0 = 0$ to $x_N = L$.

$$h_r(x) = h_N(x) = h_0(x + L), \quad 0 \le x \le L, \tag{6}$$

and the final reconstruction results of $h_r(x)$ are presented in Section 4. The reconstruction procedure is carried out within the region $x \in [0, L]$, between the source and the receiver, referred to as the *reconstruction domain*. At each stage, the receiver measures the phaseless total field, and the goal is to recover the surface height at $x = L$, i.e., $h_j(x_N)$, which corresponds to the value $h_r(x_j)$ on the target rough surface. Similarly, we define the space of the surface points at stage t_j to be Γ_j with $\Gamma_j := \{(x, z)|z = h_j(x),\ 0 \le x \le L\}$ and the upper medium to be V_j^+ with $V_j^+ := \{(x, z)|z > h_j(x),\ 0 \le x \le L\}$.

3. RECONSTRUCTION ALGORITHM

At stage t_j ($j = 1, \dots, N$), the reconstruction algorithm operates in two steps: (i) recovery of the surface current (J for the TE field and K for the TM field), and (ii) reconstruction of the surface profile at $x = L$. At reconstruction stage t_j, the surface profile $h_j(x)$ is known at grid points $x_0, x_1, \dots, x_{N-1}$, while the surface height at x_N remains unknown and needs to be determined, i.e., the target rough surface at point x_j, $h_r(x_j)$. The phaseless total field data at the receiver are measured and available for all stages in advance.

A. Step I: Recovery of the Surface Current

In the case of the TE field, at each stage t_j ($j = 1, 2, \dots, N$), the discretized form of Eq. (2a) can be written as

$$E_i(\mathbf{r_n}) = -\sum_{l=1}^{n} \int_{x_{l-1}}^{x_l} G(\mathbf{r_n}; \mathbf{r}')J(\mathbf{r}')\,\mathrm{d}x', \quad \mathbf{r_n}, \mathbf{r}' \in \Gamma_j \tag{7}$$

for the points $\mathbf{r_n} = (x_n, h_j(x_n))$ and $\mathbf{r}' = (x', h_j(x'))$. To compute the surface current J at the discrete points, we transform the above equation to a linear system:

$$\mathbf{E} = A_E\mathbf{J}, \tag{8}$$

where $\mathbf{E}, \mathbf{J} \in \mathbb{C}^N$ are two vectors of the incident electric field and the unknown surface current with elements $[\mathbf{E}]_n = E_i(\mathbf{r_n})$ and $[\mathbf{J}]_n = J(\mathbf{r_n})$, and $A_E \in \mathbb{C}^{N\times N}$ is a matrix with

$$[A_E]_{nl} = -\int_{x_{l-1}}^{x_l} G(\mathbf{r_n}; \mathbf{r}')\mathrm{d}x', \quad l \le n, \quad \mathbf{r_n}, \mathbf{r}' \in \Gamma_j \tag{9}$$

for $n = 1, 2, \dots, N$. Clearly, the matrix A_E is lower-triangular, which allows for an efficient solution of the linear system. The integrals in the matrix A_E are evaluated numerically using the standard trapezoidal rule. It is noted that the diagonal entries of A_E contain weak singularities; a treatment for evaluating these terms is described in Appendix A. Once the linear system is solved, the surface current J (surface wave derivative) is obtained along the reconstruction domain for the current stage t_j.

In the case of the TM field, at stage t_j ($j = 1, 2, \dots, N$), the discretized form of Eq. (4a) is expressed as

$$H_i(\mathbf{r_n}) = \sum_{l=1}^{n} \int_{x_{l-1}}^{x_l} \frac{\partial G}{\partial z'}(\mathbf{r_n}; \mathbf{r}')K(\mathbf{r}')\,\mathrm{d}x', \quad \mathbf{r_n}, \mathbf{r}' \in \Gamma_j, \quad \mathbf{r_n}, \mathbf{r}' \in \Gamma_j. \tag{10}$$

Similarly, this gives rise to a linear system in the form

$$\mathbf{H} = A_M\mathbf{K}, \tag{11}$$

where $\mathbf{H}, \mathbf{K} \in \mathbb{C}^N$ are vectors of the incident magnetic field and the surface current (i.e., surface wave field), respectively, with components $[\mathbf{H}]_n = H_i(\mathbf{r_n})$ and $[\mathbf{K}]_n = K(\mathbf{r_n})$, and $A_M \in \mathbb{C}^{N\times N}$ is a matrix with entries

$$[A_M]_{nl} = \int_{x_{l-1}}^{x_l} \frac{\partial G}{\partial z'}(\mathbf{r_n}; \mathbf{r}')\,\mathrm{d}x', \quad l \le n, \tag{12}$$

for $n = 1, 2, \dots, N$. As before, the integrals for the off-diagonal entries are evaluated using the trapezoidal rule, while the diagonal terms involve weak singularities, which are treated as described in Appendix B. The surface current K (surface total wave) is recovered by solving the linear system.

This procedure is carried out at each reconstruction stage t_j for $j = 1, 2, \cdots, N$. In the above formulation, evaluating the integrals in A_E and A_M requires knowledge of the surface profile $h_j(x)$ over the reconstruction domain. At this stage, the surface height is known at all previously reconstructed points $x_0, x_1, \dots, x_{N-1}$, but remains unknown at the last point x_N. To proceed, we temporarily approximate $h_j(x_N) = 0$ at each stage t_j in Step I, which allows the integrals to be computed and the linear systems to be assembled. The true value of $h_j(x_N)$ will subsequently be recovered in Step II. Although a linear system must be solved at each stage, the matrices A_E and A_M are both lower-triangular, allowing for efficient computation.

B. Step II: Reconstruction of the Rough Surface

After the surface currents have been calculated at all the discrete points along the reconstruction domain, the second integral equation [Eq. (2b) for TE or Eq. (4b) for TM] is used at each reconstruction stage t_j to recover the surface height at $x = L$, which corresponds to the target rough surface at point x_j i.e., $h_r(x_j)$. Denote the point of receiver $\mathbf{q_N} := (x_N, z_0)$.

For the TE case, at reconstruction stage t_j ($j = 1, 2, \dots, N$), the total electric field at the receiver point is measured, denoted as $E_{\mathrm{tot}} := E(\mathbf{q_N}, z_0)$. The discretized form of Eq. (2b) is written as

$$\begin{aligned} E_s(\mathbf{q_N}) &= \int_0^{x_N} G(\mathbf{q_N}; \mathbf{r}')J(\mathbf{r}')\,\mathrm{d}x' \\ &= \sum_{l=1}^{N} \int_{x_{l-1}}^{x_l} G(\mathbf{q_N}; \mathbf{r}')J(\mathbf{r}')\,\mathrm{d}x', \quad \mathbf{q_N} \in V_j^+, \mathbf{r}' \in \Gamma_j. \end{aligned} \tag{13}$$

Using the Euler's formula, the last integral (corresponding to $l = N$) is approximated using the midpoint:

$$\begin{aligned} &\int_{x_{N-1}}^{x_N} \frac{\alpha}{\sqrt{x_N - x'}} \exp\left[\frac{ik(z_0 - h_j(x'))^2}{2(x_N - x')}\right] J(\mathbf{r}')\mathrm{d}x' \\ &\quad \approx \alpha\sqrt{2\Delta x}J(\mathbf{r_N})\left[\cos I_N + i \sin I_N\right], \end{aligned} \tag{14}$$

where $\alpha = 1/2\sqrt{i/2\pi k}$, and I_N is given by

$$I_N = \frac{k(z_0 - h_j(x_N))^2}{\Delta x}. \tag{15}$$

Here, I_N contains the unknown surface height $h_j(x_N)$ to be recovered, and we aim to obtain the value of I_N. The total field at the receiver point can thus be expressed in the form

$$E_{\text{tot}} = E_i + S_N + \alpha\sqrt{2\Delta x}J(x_N)\,(\cos I_N + i\sin I_N)\,, \tag{16}$$

where E_i is the incident field at the receiver point and $S_N = \sum_{n=1}^{N-1}\int_{x_{n-1}}^{x_n} G(\mathbf{q_N};\mathbf{r}')J(\mathbf{r}')\mathrm{d}x'$. Taking the modulus and squaring both sides, and applying the identity $|z_1+z_2|^2 = |z_1|^2 + |z_2|^2 + 2\mathrm{Re}\{z_1\overline{z_2}\}$ yields

$$\begin{aligned}|E_{\text{tot}}|^2 &= |E_i + S_N|^2 + 2|\alpha|^2\Delta x|J(x_N)|^2 \\ &\quad + 2\mathrm{Re}\left\{(\overline{E_i + S_N})\cdot\alpha\sqrt{2\Delta x}J(x_N)[\cos I_N + i\sin I_N]\right\}.\end{aligned} \tag{17}$$

Applying the identity $\mathrm{Re}\{z_1z_2\} = \mathrm{Re}\{z_1\}\mathrm{Re}\{z_2\} - \mathrm{Im}\{z_1\}\mathrm{Im}\{z_2\}$, we rewrite the last term as

$$\begin{aligned}&\mathrm{Re}\left\{(\overline{(E_i + S_N)}\cdot\alpha\sqrt{2\Delta x}J(x_N)[\cos I_N + i\sin I_N]\right\} \\ &= \mathrm{Re}\left\{\alpha\sqrt{2\Delta x}J(x_N)\overline{(E_i + S_N)}\right\}\cos I_N \\ &\quad - \mathrm{Im}\left\{\alpha\sqrt{2\Delta x}J(x_N)\overline{(E_i + S_N)}\right\}\sin I_N.\end{aligned} \tag{18}$$

As the modulus of the total field and the incident field are known, then a trigonometric equation of I_N is derived with

$$a_N\cos I_N + b_N\sin I_N = c_N, \tag{19}$$

where

$$\begin{aligned}a_N &= 2\mathrm{Re}\left\{\alpha\sqrt{2\Delta x}J(x_N)\overline{(E_i + S_N)}\right\} \\ b_N &= -2\mathrm{Im}\left\{\alpha\sqrt{2\Delta x}J(x_N)\overline{(E_i + S_N)}\right\} \\ c_N &= |E_{\text{tot}}|^2 - |E_i + S_N|^2 - 2|\alpha|^2\Delta x|J(x_N)|^2.\end{aligned} \tag{20}$$

The equation can be solved by transforming it to

$$\cos(I_N - \gamma) = \frac{c_N}{\sqrt{a_N^2 + b_N^2}}, \tag{21}$$

where $\gamma = \arctan(b_N/a_N)$.

In the TM case, at the reconstruction stage t_j, the total magnetic field at the receiver point is denoted by $H_{\text{tot}} := H(\mathbf{q_N})$. The scattered magnetic field at the receiver point $\mathbf{q_N}$ is given by

$$\begin{aligned}H_s(\mathbf{q_N}) &= -\int_0^{x_N}\frac{\partial G}{\partial z'}(\mathbf{q_N};\mathbf{r}')K(\mathbf{r}')\,\mathrm{d}x' \\ &= -\sum_{l=1}^{N}\int_{x_{l-1}}^{x_l}\frac{\partial G}{\partial z'}(\mathbf{q_N};\mathbf{r}')K(\mathbf{r}')\,\mathrm{d}x'.\end{aligned} \tag{22}$$

Again, the last integral ($l = N$) can be approximated directly by

$$\begin{aligned}&\int_{x_{N-1}}^{x_N}\frac{\partial G}{\partial z'}(\mathbf{q_N};\mathbf{r}')K(\mathbf{r}')\,\mathrm{d}x' \\ &\approx \frac{2\sqrt{2}\beta}{\sqrt{\Delta x}}(z_0 - h(x_N))K(\mathbf{r_N})\,(\cos I_N + i\sin I_N)\,,\end{aligned} \tag{23}$$

where I_N is defined in Eq. (15). Unlike the TE case, the unknown surface height $h(x_N)$ appears both inside I_N and as a linear factor $(z_0 - h(x_N))$. To deal with it, we substitute $z_0 - h(x_N) = \sqrt{I_N\Delta x/k}$, then the total magnetic field at the receiver point becomes

$$H_{\text{tot}} = H_i + T_N - \frac{2\sqrt{2}\beta}{\sqrt{\Delta x}}\sqrt{\frac{I_N\Delta x}{k}}K(\mathbf{r_N})\,(\cos I_N + i\sin I_N)\,, \tag{24}$$

where H_i is the incident field at the receiver point and $T_N = -\sum_{n=1}^{N-1}\int_{x_{n-1}}^{x_n}\frac{\partial G}{\partial z'}(\mathbf{q_N};\mathbf{r}')K(\mathbf{r}')\mathrm{d}x'$. Taking the modulus and squaring both sides yields

$$\begin{aligned}|H_{\text{tot}}|^2 &= |H_i + T_N|^2 + \frac{8|\beta|^2}{k}|K(\mathbf{r_N})|^2 I_N \\ &\quad + 2\mathrm{Re}\left\{-2\sqrt{2}\beta(\overline{H_i + T_N})\sqrt{\frac{I_N}{k}}K(\mathbf{r_N})\,(\cos I_N + i\sin I_N)\right\}.\end{aligned} \tag{25}$$

Similar treatment is applied here; the real part can be expanded as

$$\begin{aligned}&\mathrm{Re}\left\{-2\sqrt{2}\beta(\overline{H_i + T_N})\sqrt{\frac{I_N}{k}}K(\mathbf{r_N})\,(\cos I_N + i\sin I_N)\right\} \\ &= \mathrm{Re}\left\{-2\sqrt{2}\beta(\overline{H_i + T_N})\frac{K(\mathbf{r_N})}{\sqrt{k}}\right\}\sqrt{I_N}\cos I_N \\ &\quad - \mathrm{Im}\left\{\mathrm{Re}\left\{-2\sqrt{2}\beta(\overline{H_i + T_N})\frac{K(\mathbf{r_N})}{\sqrt{k}}\right\}\right\}\sqrt{I_N}\sin I_N.\end{aligned} \tag{26}$$

This leads to the following algebraic equation:

$$a_N\sqrt{I_N}\cos I_N + b_N\sqrt{I_N}\sin I_N = c_N - d_N I_N, \tag{27}$$

where

$$\begin{aligned}a_N &= 2\mathrm{Re}\left\{-2\sqrt{2}\beta(\overline{H_i + T_N})\frac{K(\mathbf{r_N})}{\sqrt{k}}\right\} \\ b_N &= 2\mathrm{Im}\left\{\mathrm{Re}\left\{-2\sqrt{2}\beta(\overline{H_i + T_N})\frac{K(\mathbf{r_N})}{\sqrt{k}}\right\}\right\} \\ c_N &= |H_{\text{tot}}|^2 - |H_i + T_N|^2 \\ d_N &= 8|\beta|^2\frac{|K(\mathbf{r_N})|^2}{k}.\end{aligned} \tag{28}$$

Equation (27) can be solved by the Newton–Raphson method with an iterative process:

$$I_N \longleftarrow I_N - \frac{f(I_N)}{f'(I_N)}, \tag{29}$$

where

$$f(I_N) = a_N\sqrt{I_N}\cos I_N + b_N\sqrt{I_N}\sin I_N - c_N + d_N I_N,$$

$$f'(I_N) = a_N\left(\frac{\cos I_N}{2\sqrt{I_N}} - \sqrt{I_N}\sin I_N\right) + b_N\left[\frac{\sin I_N}{2\sqrt{I_N}} + \sqrt{I_N}\cos I_N\right] + d_N. \tag{30}$$

C. Summary of the Reconstruction Algorithm

The reconstruction proceeds through a sequence of stages $t_1, t_2, \ldots, t_N$. At each stage, the rough surface shifts by Δx toward the negative x direction, while the reconstruction is performed within the fixed reconstruction domain $x \in [0, L]$. At each reconstruction stage t_j, the surface profile is recovered at the rightmost location $x_N = L$, yielding the surface value $h_j(x_N)$, which corresponds to the target rough surface height $h_r(x_j)$. By repeating this process sequentially for $j = 1, 2, \ldots, N$, the entire rough segment $h_r(x)$ over the domain $[0, L]$ is reconstructed point by point from left to right. Therefore, the reconstruction algorithm operates in a marching manner.

The algorithm at each stage consists of two steps. In Step I, the surface current is recovered by solving a linear system [Eq. (8) for the TE case and Eq. (11) for the TM case]. Since the surface height at x_N is unknown during this step, we temporarily assume $h_j(x_N) = 0$ in order to evaluate the integrals that define the system matrix. In Step II, the quantity I_N [Eq. (15)] is computed using the obtained surface current and the measured phaseless total field data at the receiver. The resulting surface profile at x_N is given by

$$h_r(x_j) := h_j(x_N) = z_0 - \sqrt{\frac{I_N \Delta x}{k}}, \tag{31}$$

provided that the measurement height z_0 is always greater than the rough surface height.

By repeating this two-step procedure sequentially for all stages t_1 through t_N, the entire rough segment profile of the extended surface is recovered point by point along the reconstruction domain. This is in contrast to our previous related methods [21,27]; the surface current at each stage is constructed based on the successively recovered surface profile during the marching process. This constitutes a forward-marching algorithm for reconstructing rough surfaces from phaseless total field data.

The overall marching reconstruction procedure is illustrated in Algorithm 1.

Algorithm 1. Marching Reconstruction Algorithm from Phaseless Total Field Data

Input: Phaseless total field data at receiver (L, z_0) for stages $t_1, \ldots, t_N$, $|E_{\text{tot}}|$ or $|H_{\text{tot}}|$
Output: Reconstructed target rough surface profile $h_r(x)$, $0 \le x \le L$
for $j = 1$ to N **do** ▷ March through reconstruction stages t_j
  Step I: Recovery of surface current
    (a) At stage t_j, construct $h_j(x_n)$ for $n = 0, \ldots, N-1$ using the output from previous stages
    (b) Assume temporarily $h_j(x_N) = 0$
    (c) Recover surface current along the reconstruction domain by solving the linear system Eq. (8) for TE case and Eq. (11) for TM case
  Step II: Reconstruction of surface profile at x_N
    (a) Use recovered current and total field magnitude at receiver to construct equations Eq. (19) (TE) and Eq. (27) (TM)
    (b) Obtain I_N by solving corresponding equation
    (c) Recover $h_j(x_N) = z_0 - \sqrt{I_N \Delta x/k}$
  Update: Set $h_r(x_j) = h_j(x_N)$ and $h_{j+1}(x_n) = h_j(x_{n+1})$ for $n = 0, 1, \ldots, N-1$
return Reconstructed rough surface $h_r(x)$ for $x \in [0, L]$

4. NUMERICAL EXAMPLES

In this section, we present a series of numerical examples to demonstrate the performance and robustness of the proposed reconstruction algorithm. The surface is illuminated by a time-harmonic Gaussian beam (reference parabolic one) located at the point $(0, \zeta)$, with the incident field given by

$$\psi_i(x, z) = \frac{w}{(w^2 + 2ix/k)^{1/2}} \exp\left[-\frac{(z-\zeta)^2}{w^2 + 2ix/k}\right], \tag{32}$$

where w is the beam width, and k is the wavenumber. We set the wavenumber to be $k = 1$, corresponding to the wavelength being $\lambda = 2\pi$. The beam width is fixed with $w = \lambda$. The extended surface lies over the interval $[0, 2L]$ with $L = 30\lambda$, consisting of a flat segment $[0, L]$ and a rough segment $[L, 2L]$ to be reconstructed. What we present here is the final recovered profile $h_r(x)$ for $0 \le x \le L$, corresponding to the desired rough segment. The rough surface is randomly generated for each experiment from a Gaussian random process with the autocorrelation function:

$$\rho(x - x') = \sigma^2 \exp\left[-\frac{(x-x')^2}{l^2}\right], \tag{33}$$

where σ is the standard deviation of the surface height, and l represents the surface scale (correlation length) controlling the oscillation scale. In all the experiments, the surface profile has mean zero and is normalized to lie within $[-0.2\lambda, 0.2\lambda]$. The reconstruction domain $[0, L]$ is discretized using N uniform discrete grid points. At each reconstruction stage, the surface shifts by $\Delta x = \lambda/N$ to the left, while the receiver remains fixed at (L, z_0) to record the amplitude of the total field. In the TM case, the Newton method is employed to solve the nonlinear equation [Eq. (27)]. The initial guess is set to zero at the first stage and is updated using the previously reconstructed height at each subsequent stage. A fixed number of five iterations is used at each stage.

To test the robustness, reconstructions are also performed with noisy measurements. The noise is introduced by perturbing the phaseless total field Ψ according to the formula

$$\Psi^{\text{noise}} = \Psi(1 + \delta \cdot \epsilon), \tag{34}$$

where δ represents the noise level and ϵ is a random number uniformly distributed in $[-1, 1]$. This model introduces multiplicative uniform noise into the amplitude measurements, where the perturbation level is controlled by the parameter δ. The reconstruction accuracy is quantified using the relative ℓ_2-norm error:

$$e = \frac{\| H^{\text{recon}} - H^{\text{actual}} \|_2}{\| H^{\text{actual}} \|_2}, \tag{35}$$

where H^{recon} and H^{actual} denote the reconstructed and true surface profiles, respectively. The reconstruction error is computed as the average relative ℓ_2-norm error over 50 independent simulation trials, each with a randomly generated surface profile. All quantities in the algorithm are treated as complex-valued, and the final surface profile is obtained by taking the real part.

A. Reconstruction with Noise-Free Data

We first examine the performance of the proposed algorithm using non-noisy phaseless total field data. The reconstruction is carried out with $N = 512$ grid points, measurement height $z_0 = 0.7\lambda$, and surface scale $l = \lambda$. The results for both TE and TM cases are shown in Fig. 3, where the reconstructed surfaces are compared against the actual surface profiles.

As observed, the reconstructed surfaces closely match the actual ones. The main discrepancies appear near the peaks and troughs, where the curvature is high, leading to numerical instability and reduced accuracy in the reconstruction. It is also noted that the reconstruction in the TM case is slightly less accurate than in the TE case, particularly near sharp features. Overall, the method performs accurately in the noise-free setting, validating its effectiveness under ideal measurement conditions.

B. Reconstruction under Noisy Measurements

We investigate the robustness of the reconstruction algorithm in the presence of measurement noise. Specifically, if a 3% level random noise is added to the phaseless total field data, and the test is conducted with discretization size $N = 512$, measurement height $z_0 = 0.7\lambda$, and surface scale $l = \lambda$, the reconstructed surface profile for the TE case is shown in Fig. 4(a).

It is found that the recovered profile exhibits spurious oscillations induced by the noise. However, the size of these oscillations is similar to the noise level and does not obscure the key geometric features of the underlying surface, which are still well captured by the algorithm. To further reduce the effect of noise, we apply a low-pass FFT-based filter to the recovered surface. The filtered results, shown in Fig. 4(b), demonstrate good

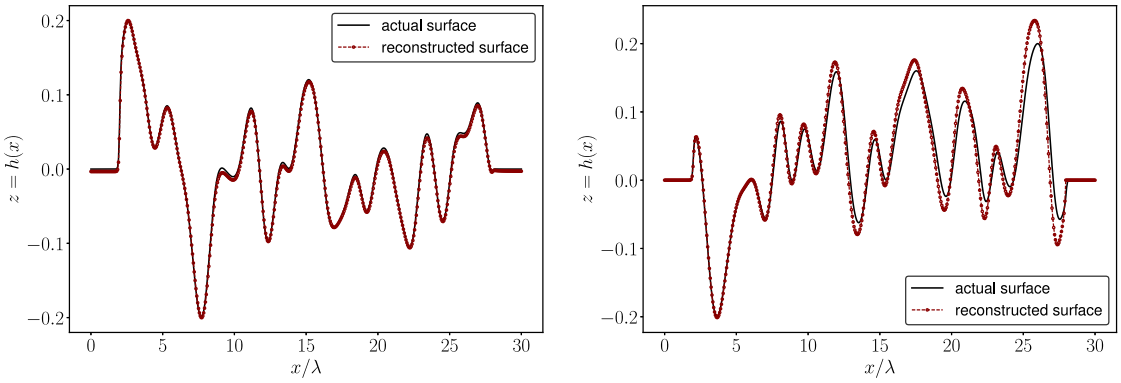

Fig. 3. Comparison of reconstructed and actual surface profiles using phaseless total field data (noise-free) for both TE and TM polarizations, with parameters set to $N = 512$, $z_0 = 0.7\lambda$, and $l = \lambda$.

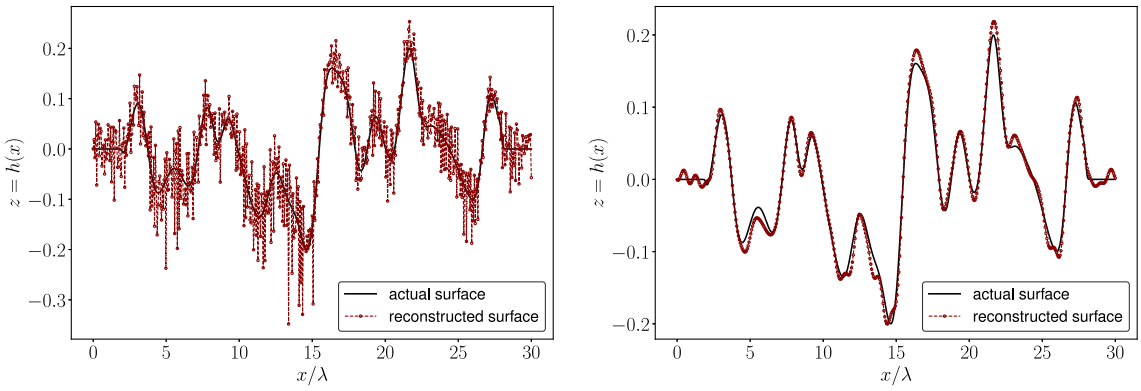

Fig. 4. Reconstructed surface versus the actual surface using 3% noisy phaseless data for the TE case with parameters set to $N = 512$, $z_0 = 0.7\lambda$, and $l = \lambda$: (a) original recovered surface without post-processing; (b) result after applying a low-pass FFT filter.

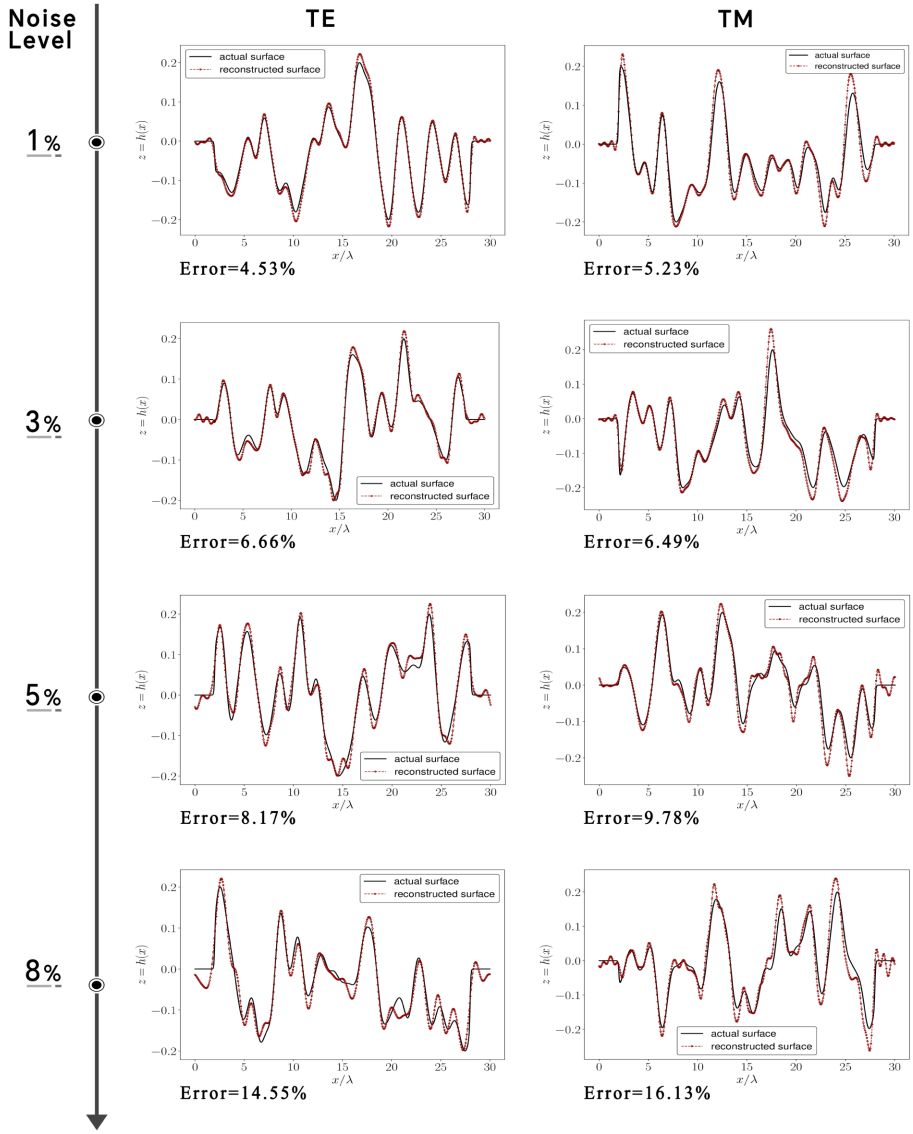

Fig. 5. Filtered reconstructed surfaces compared to the actual surface profiles under different noise levels, with the corresponding relative ℓ_2-norm reconstruction errors listed.

agreement with the true surface profiles. In the present work, FFT is used as a post-processing step to suppress high-frequency components in the reconstructed profile. Since the marching reconstruction introduces noise progressively along the spatial direction, this provides an effective and stable smoothing of the reconstruction results.

We further evaluate the algorithm's performance under noisy measurements with varying noise levels: 1%, 3%, 5%, and 8%. All tests are carried out with the same parameter setting: $N = 512$, $z_0 = 0.7\lambda$, and $l = \lambda$. The filtered reconstructed surfaces are presented in Fig. 5, with the corresponding relative ℓ_2-norm error listed. As expected, the reconstruction error increases with the noise level. Nonetheless, the algorithm remains stable and effective, and the overall surface shape is still accurately recovered. The results demonstrate that the method performs reliably under moderate noise conditions, particularly when the noise level is below 5%.

In addition, we compare the present method with the full-field method [27] under the same single-receiver moving-surface configuration. From the reconstructed profiles, both methods produce visually accurate results, with no significant degradation observed in the present method. The reconstruction errors for both methods under different noise levels are summarized in Table 2. It is shown that, although the full-field method generally achieves slightly lower errors, the present method produces comparable reconstruction accuracy across all noise levels. This indicates that the proposed method remains effective despite relying only on phaseless data and confirms its capability in a more restrictive and practically relevant measurement setting.

C. Sensitivity to Problem Parameters

In the following tests, we assess the sensitivity of the reconstruction algorithm to key problem parameters. In all experiments, a

Table 2. Comparison of Reconstruction Errors (%) for the Present Method and the Previous Full-Field Method under the Same Single-Receiver Moving-Surface Setting, with Parameters $N = 512$, $z_0 = 0.7\lambda$, and $l = \lambda$, for Both TE and TM Cases at Different Noise Levels

	Ref. [27] (Full Field)		Proposed Method (Phaseless Data)	
Noise Level (%)	TE	TM	TE	TM
0	3.97	4.15	4.51	5.11
3	6.74	5.69	6.66	6.49
5	7.54	8.49	8.17	9.78

Table 3. Relative Reconstruction Error under Different Receiver Heights z_0 Using 3% Noisy Data with Discretization Size $N = 512$ and Surface Scale $l = \lambda$

z_0/λ	TE Error (%)	TM Error (%)
0.5	6.40	6.75
0.7	6.66	6.49
1.0	6.28	7.08
1.5	6.85	7.60

Table 4. Relative Reconstruction Error with Respect to Different Numbers of Grid Points N Using 3% Noisy Data with Measurement $z_0 = 0.7\lambda$ and Surface Scale $l = \lambda$

N	TE Error (%)	TM Error (%)
256	8.24	8.39
384	7.80	8.12
512	6.66	6.49
768	5.37	6.15

3% level of noise is applied to the phaseless total field data, and the results are obtained by applying the low-pass FFT-based filter to the recovered surface. The reported reconstruction errors are also computed based on the filtered surfaces.

We first examine the effect of the receiver height z_0, which is the measurement distance from the surface. In this test, all other parameters are fixed as before: the discretization size is set to $N = 512$, and the surface scale is $l = \lambda$. It is observed that the recovered surfaces remain similar to the noise-free case across different values of z_0, with the main surface features well preserved. The relative ℓ_2-norm reconstruction error corresponding to different measurement heights z_0 is reported in Table 3 for both TE and TM cases.

The results show that the algorithm remains stable across a range of values of receiver height, with only mild variations in accuracy. It indicates the method's robustness with respect to the receiver's vertical placement.

The effect of the number of grid points N on reconstruction accuracy is examined here. This test is conducted under the same setting as before using 3% noisy data with receiver height $z_0 = 0.7\lambda$ and surface scale $l = \lambda$. The visual plots show no significant differences across different values of N, and the main geometric features are consistently recovered. The relative reconstruction error is listed in Table 4 for using different values of N.

As expected, the accuracy improves gradually as N increases due to finer spatial resolution.

The influence of the horizontal surface scale l, which controls the oscillatory nature of the rough surface, is also examined. A smaller l leads to finer surface variations and requires a higher discretization resolution to resolve accurately. Figure 6 shows the reconstructed surface with a finer surface scale $l = \frac{2}{3}\lambda$, obtained using 3% noisy data, a discretization size of $N = 512$, and a receiver height of $z_0 = 0.7\lambda$.

The main structure of the surface is still well captured, although discrepancies become more pronounced near sharp peaks and troughs where the surface varies more rapidly.

To further quantify the impact of surface scale l and discretization resolution N, we present the relative ℓ_2-norm error with respect to various combinations of l and N in Table 5.

As shown, more oscillatory surfaces (smaller l) result in higher reconstruction error, particularly when the number of discretization points is insufficient. However, by increasing the resolution N, the reconstruction accuracy improves for both TE and TM cases. This indicates that the algorithm can adapt to finer surface structures when adequately resolved.

5. CONCLUSION

In this paper, we have developed a reconstruction algorithm for recovering rough surface profiles using phaseless total field data measured at a single receiver. This work extends our previous

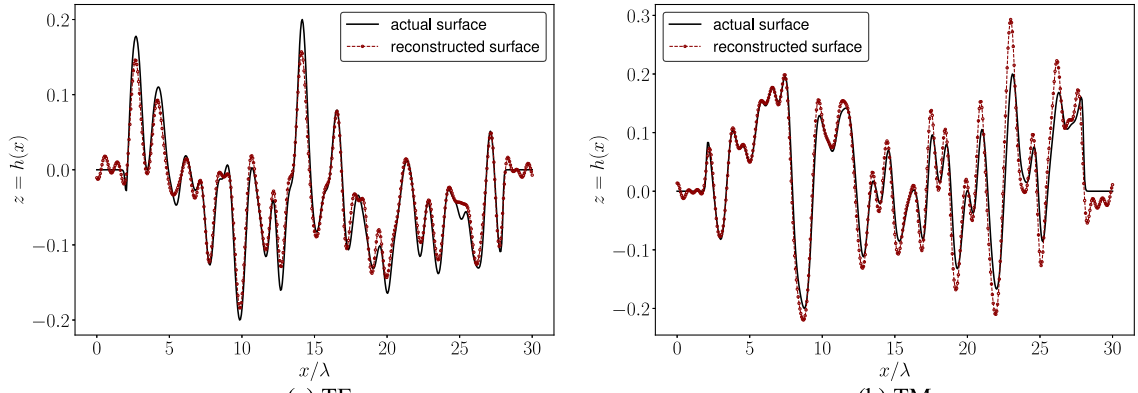

(a) TE (b) TM

Fig. 6. Filtered reconstructed surfaces compared to the actual surfaces for TE and TM cases, using 3% noisy data with finer surface scale $l = \frac{2}{3}\lambda$.

Table 5. Relative Reconstruction Errors under 3% Noisy Data for Different Surface Scales l and Discretization Sizes N, with Receiver Height $z_0 = 0.7\lambda$

Surface Scale l/λ	Grid Points N	TE Error (%)	TM Error (%)
1.5	384	5.60	5.12
1.0	512	6.66	6.49
2/3	512	8.76	9.03
2/3	768	8.01	8.14
0.5	512	13.28	13.36
0.5	768	12.27	13.12
0.5	1024	10.87	11.54

study [27], which addressed the same problem using full phase information. The method is formulated under the parabolic wave equation framework and considers both TE (Dirichlet) and TM (Neumann) polarizations. As the surface undergoes controlled lateral shifts, the algorithm proceeds in a marching fashion: at each stage, the surface current is first approximated, followed by the recovery of the surface height at the receiver point. This sequential strategy enables efficient and progressive reconstruction of the entire rough segment.

A series of numerical examples were presented to validate the effectiveness and robustness of the proposed approach. The results demonstrate accurate reconstruction of surface profiles in both TE and TM cases, with the main geometric features well recovered under both noise-free and noisy measurements. Further tests were conducted to assess the sensitivity of the method with respect to key problem parameters, including receiver height, discretization resolution, and surface roughness scale. Across all tested scenarios, the reconstructed surfaces remained consistent with the true profiles, confirming the reliability and adaptability of the algorithm.

While this work is limited to two-dimensional problems, there are several potential directions for further development. Extending the algorithm to three-dimensional surface reconstruction poses significant computational challenges but would greatly enhance its practical applicability. The algorithm could also be adapted to more complex configurations such as waveguide environments [33], where multiple scattering effects are more pronounced. Furthermore, integrating data-driven techniques such as deep learning-based solvers [34,35] may further enhance the reconstruction accuracy and efficiency, especially under limited or noisy measurements.

APPENDIX A: TREATMENT OF SINGULAR INTEGRAL IN EQ. (9)

The diagonal entry of the matrix A_E in Eq. (9) involves weakly singular integrals of the form

$$-\int_{x_{n-1}}^{x_n} \frac{\alpha}{\sqrt{x_n - x'}} \exp\left[\frac{ik}{2}\frac{(h(x_n)-h(x'))^2}{x_n - x'}\right] \mathrm{d}x'. \quad \textbf{(A1)}$$

We first approximate the surface height $h(x')$ locally by its first-order expansion at x_n: $h(x') \sim h(x_n) + h'(x_n)(x' - x_n)$, the integral becomes

$$-\int_{x_{n-1}}^{x_n} \frac{\alpha}{\sqrt{x_n - x'}} \exp\left[\frac{ik}{2}h'(x_n)^2(x_n - x')\right] \mathrm{d}x'. \quad \textbf{(A2)}$$

Next, we apply a linear approximation to the exponential term by $1 + \frac{ik}{2}h'(x_n)^2(x_n - x')$, the integral then becomes a sum of two elementary integrals:

$$-\int_{x_{n-1}}^{x_n} \frac{\alpha}{\sqrt{x_n - x'}}\mathrm{d}x' - \int_{x_{n-1}}^{x_n} \alpha\frac{ik}{2}h'(x_n)^2\sqrt{x_n - x'}\mathrm{d}x', \quad \textbf{(A3)}$$

and both terms can be evaluated in closed form, leading to the final result:

$$[A_E]_{nn} = -2\alpha\sqrt{\Delta x} - \frac{ik\alpha}{3}h'(x_n)^2\Delta x^{3/2}. \quad \textbf{(A4)}$$

APPENDIX B: TREATMENT OF SINGULAR INTEGRAL IN EQ. (12)

The singular integral in the diagonal entry of the matrix A_M reads

$$\int_{x_{n-1}}^{x_n} \beta\frac{h(x_n) - h(x')}{(x_n - x')^{3/2}} \exp\left[\frac{ik}{2}\frac{(h(x_n)-h(x'))^2}{x_n - x'}\right] \mathrm{d}x'. \quad \textbf{(B1)}$$

Using the same linear approximation to the surface height and expanding the exponential to first order, the integral reduces to

$$\int_{x_{n-1}}^{x_n} \frac{\beta h'(x_n)}{\sqrt{x_n - x'}}\mathrm{d}x' + \int_{x_{n-1}}^{x_n} \beta\frac{ik}{2}h'(x_n)^3\sqrt{x_n - x'}\mathrm{d}x'. \quad \textbf{(B2)}$$

This gives rise to the closed-form expression

$$[A_M]_{nn} = 2\beta h'(x_n)\sqrt{\Delta x} + \frac{ik\beta}{3}h'(x_n)^3\Delta x^{3/2}. \quad \textbf{(B3)}$$

Funding. Natural Science Foundation of Jiangsu Province (BK20230466).

Disclosures. The authors declare no conflicts of interest.

Data availability. Data underlying the results presented in this paper are not publicly available at this time but may be obtained from the authors upon reasonable request.

REFERENCES

1. A. G. Voronovich, *Wave Scattering from Rough Surfaces* (Springer, 1999), Vol. **17**.
2. K. F. Warnick and W. C. Chew, "Numerical simulation methods for rough surface scattering," Waves Random Media **11**, R1 (2001).
3. R. E. Malkin, A. C. Franklin, R. L. Bevan, *et al.*, "Surface reconstruction accuracy using ultrasonic arrays: application to non-destructive testing," NDT&E Int. **96**, 26–34 (2018).
4. D. Liang, P. Xu, L. Tsang, *et al.*, "Electromagnetic scattering by rough surfaces with large heights and slopes with applications to microwave remote sensing of rough surface over layered media," Prog. Electromagn. Res. **95**, 199–218 (2009).
5. R. W. Deming and A. J. Devaney, "Diffraction tomography for multi-monostatic ground penetrating radar imaging," Inverse Probl. **13**, 29 (1997).
6. P. A. E. M. Janssen and P. Viterbo, "Ocean waves and the atmospheric climate," J. Clim. **9**, 1269–1287 (1996).
7. R. J. Wombell and J. A. DeSanto, "Reconstruction of rough-surface profiles with the Kirchhoff approximation," J. Opt. Soc. Am. A **8**, 1892–1897 (1991).
8. A. Schatzberg and A. J. Devaney, "Rough surface inverse scattering within the Rytov approximation," J. Opt. Soc. Am. A **10**, 942–950 (1993).

9. A. Sefer and A. Yapar, "An iterative algorithm for imaging of rough surfaces separating two dielectric media," IEEE Trans. Geosci. Remote Sens. **59**, 1041–1051 (2021).
10. I. Akduman, R. Kress, and A. Yapar, "Iterative reconstruction of dielectric rough surface profiles at fixed frequency," Inverse Probl. **22**, 939 (2006).
11. R. Kress and T. Tran, "Inverse scattering for a locally perturbed half-plane," Inverse Probl. **16**, 1541 (2000).
12. A. Yapar, O. Ozdemir, H. Sahinturk, *et al.*, "A Newton method for the reconstruction of perfectly conducting slightly rough surface profiles," IEEE Trans. Antennas Propag. **54**, 275–279 (2006).
13. P. Mojabi and J. LoVetri, "Overview and classification of some regularization techniques for the Gauss-Newton inversion method applied to inverse scattering problems," IEEE Trans. Antennas Propag. **57**, 2658–2665 (2009).
14. G. Bozza and M. Pastorino, "An inexact Newton-based approach to microwave imaging within the contrast source formulation," IEEE Trans. Antennas Propag. **57**, 1122–1132 (2009).
15. F. Qu, B. Zhang, and H. Zhang, "A novel integral equation for scattering by locally rough surfaces and application to the inverse problem: the Neumann case," SIAM J. Sci. Comput. **41**, A3673–A3702 (2019).
16. J. Li, J. Yang, and B. Zhang, "A linear sampling method for inverse acoustic scattering by a locally rough interface," Inverse Probl. Imaging **15**, 1247–1267 (2021).
17. A. Krynkin, K. V. Horoshenkov, and T. Van Renterghem, "An airborne acoustic method to reconstruct a dynamically rough flow surface," J. Acoust. Soc. Am. **140**, 2064–2073 (2016).
18. G. Dolcetti, M. Alkmim, J. Cuenca, *et al.*, "Robust reconstruction of scattering surfaces using a linear microphone array," J. Sound Vib. **494**, 115902 (2021).
19. Y. Chen and M. Spivack, "Rough surface reconstruction at grazing angles by an iterated marching method," J. Opt. Soc. Am. A **35**, 504–513 (2018).
20. Y. Chen, O. R. Spivack, and M. Spivack, "Recovery of rough surface in ducting medium from grazing angle scattered wave," J. Appl. Phys. **124**, 084901 (2018).
21. Y. Chen, O. R. Spivack, and M. Spivack, "Rough surface reconstruction from phaseless single frequency data at grazing angles," Inverse Probl. **34**, 124002 (2018).
22. M.-D. Johnson, J. Cuenca, T. Lähivaara, *et al.*, "Bayesian reconstruction of surface shape from phaseless scattered acoustic data," J. Acoust. Soc. Am. **156**, 4024–4036 (2024).
23. X. Ji, X. Liu, and B. Zhang, "Inverse acoustic scattering with phaseless far field data: uniqueness, phase retrieval, and direct sampling methods," SIAM J. Imaging Sci. **12**, 1163–1189 (2019).
24. G. Bao and L. Zhang, "Shape reconstruction of the multi-scale rough surface from multi-frequency phaseless data," Inverse Probl. **32**, 085002 (2016).
25. A. Sefer, "Locally perturbed inaccessible rough surface profile reconstruction via phaseless scattered field data," IEEE Trans. Geosci. Remote Sens. **60**, 2002808 (2022).
26. O. Ivanyshyn and R. Kress, "Inverse scattering for surface impedance from phase-less far field data," J. Comput. Phys. **230**, 3443–3452 (2011).
27. Y. Chen, M. Spivack, and O. R. Spivack, "Reconstruction of rough surfaces from a single receiver at grazing angle," IET Sci. Meas. Technol. **18**, 361–372 (2024).
28. J. A. DeSanto, "Exact boundary integral equations for scattering of scalar waves from infinite rough interfaces," Wave Motion **47**, 139–145 (2010).
29. G. S. Brown, "A scattering result for rough surfaces having small height but arbitrary slope," Wave Motion **12**, 475–483 (1990).
30. E. I. Thorsos, "Rough surface scattering using the parabolic wave equation," J. Acoust. Soc. Am. **82**, S103 (1987).
31. F. D. Tappert, "The parabolic approximation method," in *Wave Propagation and Underwater Acoustics*, J. B. Keller and J. S. Papadakis, eds. (Springer Berlin Heidelberg, 1977), pp. 224–287.
32. M. Spivack, "A numerical approach to rough-surface scattering by the parabolic equation method," J. Acoust. Soc. Am. **87**, 1999–2004 (1990).
33. Y. Yu, A. Krynkin, and K. V. Horoshenkov, "The effect of 3D surface roughness on acoustic wave propagation in a cylindrical waveguide," Wave Motion **128**, 103304 (2024).
34. Y. Chen, C. Wang, Y. Hui, *et al.*, "Surface profile recovery from electromagnetic fields with physics-informed neural networks," Remote Sens. **16**, 4124 (2024).
35. I. Aydin, G. Budak, A. Sefer, *et al.*, "CNN-based deep learning architecture for electromagnetic imaging of rough surface profiles," IEEE Trans. Antennas Propag. **70**, 9752–9763 (2022).